Boundary layer forcing on a rotating wing at low Reynolds numbers

Tomek Jaroslawski, Maxime Forte, Jean-Marc Moschetta, Erwin Ricky Gowree

Boundary layer forcing on a rotating wing at low Reynolds numbers

Tomek Jaroslawski[1*], Maxime Forte[1], Jean-Marc Moschetta[2] and Erwin Gowree[2]

[1*]Department of Multi-Physics for Energetics, ONERA, Toulouse, 31000, France.
[2]Department of External Aerodynamics and Propulsion, ISAE-SUPEARO, Toulouse, 31000, France.

*Corresponding author(s). E-mail(s): thomas.jaroslawski@onera.fr;

Abstract

Two separate experiments were conducted on a three-bladed NACA0012 rotor operating at a blade tip Reynolds number ranging from $44 - 110 \times \mathbf{10^3}$ using phase-locked infrared thermography (IRT) coupled with force and torque measurements. The first experiment consisted of a parametric study on the impact of forcing boundary layer transition using roughness placed on the suction side of the aerofoil in a hover configuration. The roughness height varied from $52-220$ $\boldsymbol{\mu}$m and was placed all at 10% chord over the entire span of the blade. Force and torque measurements revealed a roughness height that could lead to a performance increase due to the suppression or reduction of a laminar separation bubble. Moreover, IRT measurements showed the formation of turbulent wedges behind the roughness elements at critical roughness Reynolds numbers based on empirical correlations from the literature. The second set of experiments investigated the effects of freestream turbulence (FST) on the performance and flow development of the same rotor in an advancing configuration. FST was generated in an open section wind tunnel using grids and was characterised using hot-wire anemometry. When the rotor was subjected to FST, an increase in thrust and efficiency was observed, which could be due to the FST suppressing laminar flow separation by inducing early transition since IRT measurements indicated an advancement of the transition region, confirming performance improvement

with earlier transition, where the excrescence drag due the roughness elements would not be present in the freestream turbulence forcing case.

Keywords: Boundary layer transition, roughness, turbulence, drone

1 Introduction

Micro aerial vehicles (MAVs) are currently of interest for military and civil applications. These vehicles operate within a Reynolds number regime of $10^3 < Re_{tip} < 10^5$ ($Re = U_{tip}c/\nu$, where c denotes the chord, ν the kinematic viscosity and for a rotor blade: $U_{tip} = R\Omega$, where R is the blade radius, and Ω is the rotational speed). At these Reynolds numbers, one can expect that the flow remains laminar to a greater extent but is still susceptible to the transition to turbulence. MAVs are projected to fly at low altitudes and in complex terrain. Thus, they will operate in the lower levels of the atmospheric boundary layer and within the roughness zone; that is, the layer of air close to the ground, which contains the local wakes and influences of upstream objects such as buildings or trees. Therefore, understanding the effects of freestream turbulence on the boundary layer development over low Reynolds number lifting devices is of current interest.

At low and transitional Reynolds numbers, the boundary layer physics are complex, including laminar separation, transition and reattachment. For this reason, past investigations exhibit performance sensitivity to the Reynolds number. Therefore, the design and optimisation of low Reynolds number rotors and propellers are currently limited, where the effects of freestream turbulence or roughness are not used in the design process. The inability of laminar boundary layers to endure strong adverse pressure gradients results in separation, resulting in an unstable detached shear layer that undergoes the transition to turbulence. Depending on the flow conditions, the shear layer may remain separated or reattach to the aerofoil, with the former leading the aerofoil to be in a stalled state and the latter forming a closed region of recirculating flow, referred to as a laminar separation bubble (LSB)[1]. These separated flows over lifting surfaces typically lead to undesirable effects, including a decreased lift-to-drag ratio, unsteady loading, and noise.

LSBs occur over fixed and rotating aerofoils; in the current investigation, we will focus on rotating aerodynamic surfaces. A detailed review on LSBs over fixed surfaces can be found in [2, 3]. Recently, Thiessen and Shülein [4] conducted transition experiments over a low Reynolds number quadcopter rotor using infra-red thermography (IRT) and oil film interferometry measurements. They found a region of separated flow, which they claimed to be an LSB which forms over the rotor blade. The LSB is a zone of almost stationary or low-speed reverse flow, where the shear stress is zero or very low. In the separation region, the heat transfer will be minimal and increase rapidly as transition, and turbulent reattachment occurs. In general, IRT measurements

conducted on a model which has a higher surface temperature than the free stream allow for the identification of turbulent regions (low temperature, low pixel intensity, I_N), separated regions (high temperature, high values of I_N) and laminar regions (medium temperature regions). Lang et al.[5] used IRT and particle image velocimetry (PIV) to detect the presence of an LSB over a NACA 0015 rotor blade, showing that the elevated temperature region could be used to determine the location of the bubble (the local Re at which the bubble was measured was $1.4{\times}10^5$). Recent IRT measurements by Jaroslawski et al. [6] demonstrated that IRT measurements could provide qualitative quantification of the flow topology over a NACA0012 rotor, with a stagnant region of high-temperature being linked to a possible region of separated flow. High-resolution Large Eddy Simulations (LES) by Shenoy et al. [7] over the same rotor configuration as Jaroslawski et al. [6] also found the presence of an LSB. Grande et al. [8] conducted phase-locked PIV and oil-flow visualisations over a low Reynolds number propeller. Their results revealed a complex flow field with the appearance of an LSB on the suction side of the blade, which moved towards the leading edge and reduced in size as the advance ratio decreased.

In general, the presence of an LSB is associated with a decrease in performance. For example, Singh and Ahmed [9] considered an LSB when designing a low Reynolds number wind turbine and noted that LSBs over low Reynolds number rotors cause excessive pressure drag, loss in the aerodynamic lift and increase the noise produced by the rotor. However, controlling boundary layer separation has been found to have beneficial effects on performance. Jung and Baeder [10] conducted numerical simulations on a wind turbine rotor and found that forcing transition with optimally distributed surface roughness affects the performance differently depending on the state of the boundary layer. They found that in the presence of separated flows, adding upstream roughness could increase the performance up to 23.3%, whereas it would decrease by 8.3% for an attached flow. Moreover, recent numerical simulations on a rotor similar to the NASA Mars helicopter ($\mathrm{Re} \leq 1 \times 10^5$ at the blade tip) by Argus et al. [11] showed that early transition caused by a decreased critical amplification factor resulted in a thrust increase through the elimination of laminar separation. At higher Re_{tip}, the benefit of early transition diminished and became detrimental for the thrust produced by the rotor. They showed that the Figure of Merit (FM) could be increased by 40% by decreasing the N-Factor, where the N-factor measures the growth rate of the perturbation in boundary layers. Jaroslawski et al. [6] conducted force and torque measurements over a rotor where boundary layer transition was promoted using significant (relative to the boundary layer thickness) 2D and 3D roughness elements, resulting in a general decrease in performance, which was attributed to increased excrescence drag caused by the roughness elements. However, they postulated that a well-designed roughness array could improve the performance.

Further investigation of the effects of boundary layer transition over MAV rotors is required, as previous investigators [6, 9, 12] have shown that the state of the boundary layer can have a significant impact on the performance and

flow topology. Based on the author's literature review, no studies systematically investigate the effects of roughness or freestream turbulence on the flow transition and performance of a low Reynolds number rotor. Therefore, the present investigation is carried out to investigate the effects of these boundary layer forcing methods by employing two *separate* experiments. The first set of experiments consists of a parametric investigation on the rotor in a hover configuration ($U_o = 0\ m/s$, i.e., no incoming freestream velocity) subjected to forcing via 3D roughness (circular cylinders). The roughness elements were placed at $x/c = 0.1$ on the suction side of each blade and had heights (k) varying from $52-220\ \mu$m. Force and torque measurements were used to measure the performance of the rotor, and IRT was employed to measure the flow topology of the rotor. The second experiment is an exploratory study of the effects of freestream turbulence on the performance and flow development on the same low Reynolds number rotor in an advancing configuration. Freestream turbulence (FST) was generated in an open section wind tunnel in a controlled manner using square grids and was characterised using hot-wire anemometry. As in the first experiment, the flow topology and performance were measured.

The following section (Sec. 2) describes the experimental facility, the two experiments and the IRT and force measurement set-up. Next, the results are presented in Sec. 3. The flow topology of the rotor in the baseline hover configuration is characterised by comparing experimental results to past CFD studies (Sec. 3.1). Then, the results from the experiments where the boundary layer developing over the suction side of the aerofoil is forced using roughness (Sec. 3.2) or freestream turbulence (Sec. 3.3) are presented, after which some conclusions are drawn in the final section (Sec. 4).

2 Experiment and Methods

The experiments were conducted at the Institut Supérieur de l'Aéronautique et de l'Espace (ISAE-SUPAERO) with the collaboration of ONERA in Toulouse, France. The rotor had three blades with a NACA0012 profile at an angle of incidence of 10 ° fixed along the span. The radius (R) of the rotor was 0.125 m, and the chord length (c) was 0.025 m, resulting in an aspect ratio ($AR = R/c$) of 5. The rotor blades were 3D printed using a reinforced resin and polished manually, ensuring that the blade was smooth. The rotor was mounted in a recirculating open test section wind tunnel with a measured level of freestream turbulence intensity (Tu) of 0.42% (for a frequency band of $2Hz - 10kHz$ at a freestream speed of $U_o = 3.5$ m/s which was measured using a Pitot tube. The experimental setup is presented in Fig. 1. Two separate experiments were conducted:

1. The rotor in a hover configuration (U_o=0) where 3D circular roughness elements (cf. Fig.2a) were placed at $x/c = 0.1$, uniformly spaced along the entire span of the rotor and their height varying from $52 - 220\ \mu$m, all having a diameter of 1.37 mm and a standard interval length of 2.54 mm. The rotation speeds were set to 2000 – 5000 RPM.

2. The rotor in the advancing condition was subjected to a freestream flow velocity of $U_o = 3.5\ m/s$, where the rotational speeds varied from $2000 - 5000$ RPM. Regular square grids generated freestream turbulence (cf. Fig.2b) and were placed 35 cm away from the rotor.

The freestream flow conditions were measured using a 5 μm Dantec 55P11 probe operating in constant temperature mode using a DISA 55M01 anemometer system. The hotwire data was collected using a NI Compact DAQ-9178 with a 24-bit NI-9239 module at a sampling frequency of 20 kHz, with a cutoff of 10 kHz. The probe was calibrated $in - situ$ against a Pitot tube connected to an MKS 220DD pressure transducer, using King's law [13]. Data were sampled for a period that captured approximately 30000 integral lengths of the flow, resulting in a sampling time of 60 seconds. The decay of the grid-generated freestream turbulence was characterised by measuring at multiple streamwise positions before the rotor.

The performance of the rotor was determined with force and torque measurements. The thrust and torque were measured using the same aerodynamic balance as in Desert et al. [14]. The thrust was measured by fixing one end of the load cell to the motor driving the rotor and the other to a fixed support. The torque was obtained by fixing one end of the load cell to a circular plate fixed to the back of the motor (aligned with the axis of rotation) and the other to a fixed frame surrounding the motor. The frame allows for free rotation of the motor along its axis through two ball bearings. Therefore, when a torque is applied, it pushes onto the load cell. The setup measures the sum of the aerodynamic torque exerted by the rotor on the motor and the internal mechanical torque of the motor. The sampling frequency of the force and torque measurements was 500 Hz; 5000 samples were acquired, with a 10-second stabilisation period between each speed interval. The force and torque were measured for long enough so that their means and standard deviations converged. The uncertainty of the thrust and torque measurements was calculated using a 95% confidence interval; the total uncertainty for the thrust and torque was approximately 1% and 0.045 % of full scale, respectively.

The flow topology on the suction side of the aerofoil was measured using IRT. Based on the experimental setup from Jaroslawski et al. [6], phase-locked IRT was conducted to capture the temperature distribution of the rotor blade's surface. A Brüel Kjær CCLD laser tacho probe synchronised the blade with the IR Camera. A thin and reflective film was placed on an opposing blade so that a voltage pulse was sent out by the laser for each rotation, triggering the camera. The temperature difference between the ambient air and the blade's surface was increased using a 500W halogen lamp to heat the blade's surface. Before starting the measurement, the lamp systematically heated the blade at a distance of 0.15 m for 10 seconds. The room temperature was at 20 °C, and the blade was heated to approximately 35-40 °C in each case; however, the absolute temperature is not of great importance as the temperature difference suffices for transition detection. Energy injected into the flow due to heating of the blade can affect the critical Reynolds number at which boundary layer

transition occurs [15]. However, the heating is too low to affect the transition process, especially at the low Reynolds numbers studied, where the boundary layer is much more stable. In previous work, the overheat temperature employed was between 10-20 °C, where [16–18] suggested that these levels of overheat do not significantly affect the transition position.

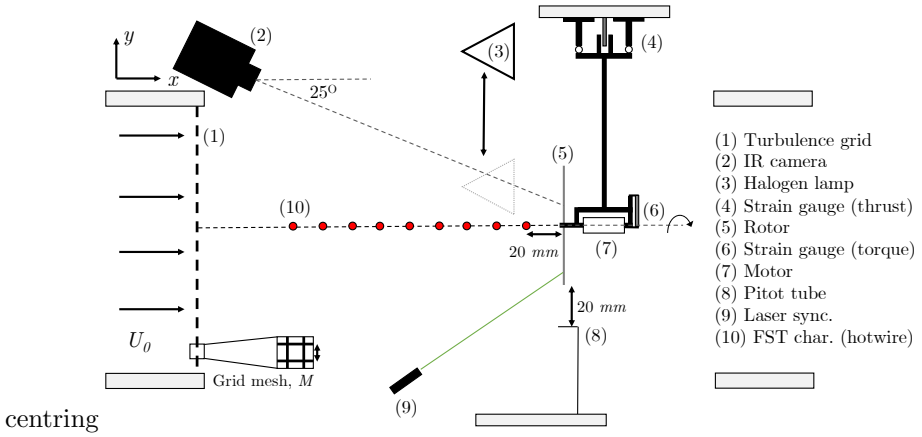

Fig. 1 Experimental Setup. NB: Open section wind tunnel. The schematic does not show a convergence section at the inlet and a divergence section at the outlet.

The Richardson number quantifies the relevance of natural convection concerning forced convection. The Richardson number is defined in Eq. 1, where θ, represents the volumetric thermal expansion coefficient ($105\times10^{-6}/C°$), the surface temperature of the model and the ambient air temperature are denoted by T_w and T_∞, respectively. We use the rotational acceleration (U_{tip}^2/r) instead of the acceleration due to gravity as the former would dominate and a velocity scale of U_{tip}, which divides out, yielding the simplified expression:

$$Ri = c\theta(T_w - T_\infty)/r \tag{1}$$

Natural convection can be considered to be negligible if $Ri < 0.1$, in the present work $Ri \sim 0.0032$ at $r/R = 0.1$ and decreases as r/R is increased; therefore, natural convection effects on the flow can be neglected.

During the IR camera measurement, the heating lamp was turned off. The motivation of this technique is that in a turbulent flow region, there will be more heat transfer between the wall and outer flow than in a laminar flow region. Each IR image was normalised by the maximum pixel intensity present in the image so that the different test configurations would be compared reliably. A high-speed and high-resolution IR camera (Infratec ImageIR 9400) was used to characterise the flow topology over the rotor, where the pixel intensity is used to approximate the state of the boundary layer. The camera had an InSB sensor with a nominal Noise Equivalent Temperature Difference (NETD)

$< 30mK$. It was positioned 0.4m away from the rotor blade and at a horizontal angle of 25° (cf. Fig.1). The reduced field of view was $1c \times 0.8R$ (170 $\times$ 520 pixels), and the camera's exposure time was 68μs, allowing for a good compromise between camera noise and motion blur. Since the camera was synchronised with the rotor, the sampling rate was that of the rotor turning rate (RPM) for the given run. Motion blur is one of the greatest challenges when conducting IR measurements over rotors, even with state-of-the-art cameras. The motion blur can be calculated by multiplying the camera's exposure time by the local radial velocity and would increase with rotational speed and radial position. For example, at the highest speed, 5000 RPM, and the blade tip, the motion blur can be up to 0.18c. However, this value is less than 0.1c for a large portion of the blade as the radial velocity decreases moving inboard. When raw images were analysed, the blur was not significant enough to affect the test result, potentially due to reliable synchronisation. Furthermore, at lower rotational speeds, the blur is between 0.01c and 0.1c, depending on speed and radial position.

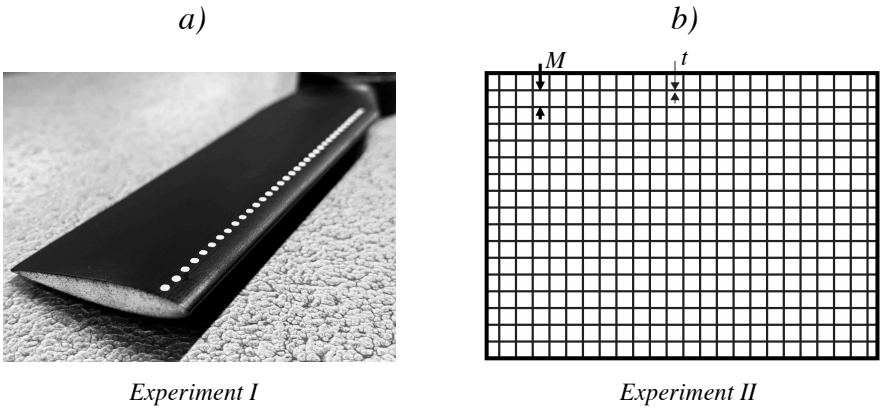

Fig. 2 Forcing methods used in the study. (a) 3D circular roughness elements. (b) 3D printed regular square grid.

The coefficient of thrust (C_T), torque (C_Q), efficiency (η), Power Loading (PL) and Figure of Merit (FM) are defined in Eqs. 2, 3,5, 4 and 6, respectively. Where T is the thrust, Q is the torque, ρ is the density of the ambient air, Ω is the rotational speed in rad/s, R is the rotor blade radius and U_0 is the incoming velocity. The advance parameter is $J = \pi U_o/\Omega R$.

$$C_T = \frac{T}{\rho(\Omega R)^2 \pi R^2} \tag{2}$$

$$C_Q = \frac{Q}{\rho(\Omega R)^2 \pi R^3} \tag{3}$$

$$PL = \frac{T}{\Omega Q} \tag{4}$$

$$\eta = \frac{TU_0}{\Omega Q} \tag{5}$$

$$FM = \frac{T^{3/2}}{\Omega Q\sqrt{2\rho\pi R^2}} \tag{6}$$

2.1 Boundary layer approximation

Due to the experimental difficulty in measuring the boundary layer thickness (δ) over a small-scale rotating surface, δ is calculated numerically. An estimation of the boundary layer thickness alows for the calculation U_k: the undisturbed velocity in the boundary layer at the roughness height. Using U_k as a velocity scale and the height of the roughness (k) as a length scale, the roughness Reynolds number is obtained, *viz*

$$Re_k = \frac{U_k k}{\nu} \tag{7}$$

The pressure over the suction side of the untripped rotor was calculated using XFOIL [19] for the local Reynolds number based on the local radial speed. The effective aerodynamic angle of attack (α_{eff}) for the corresponding radial position and rotation speed was calculated using a Non-Linear Vortex Lattice Method (NLVLM) which should take into account some of the 3D effects present; the method is explained in detail in Jo et al. [20]. Using slices of the pressure distribution for different radial positions obtained from XFOIL (calculated with an N-Factor of 7), the δ was calculated using ONERA's in-house boundary layer code 3C3D, which solves Prandtl's boundary layer equations for three-dimensional boundary layers using a method of characteristics along local streamlines. Boundary layer equations are cast in a body-fitted coordinate system, and the momentum equations are discretised along the local streamlines [21, 22]. A schematic of the method is presented in Fig. 3.

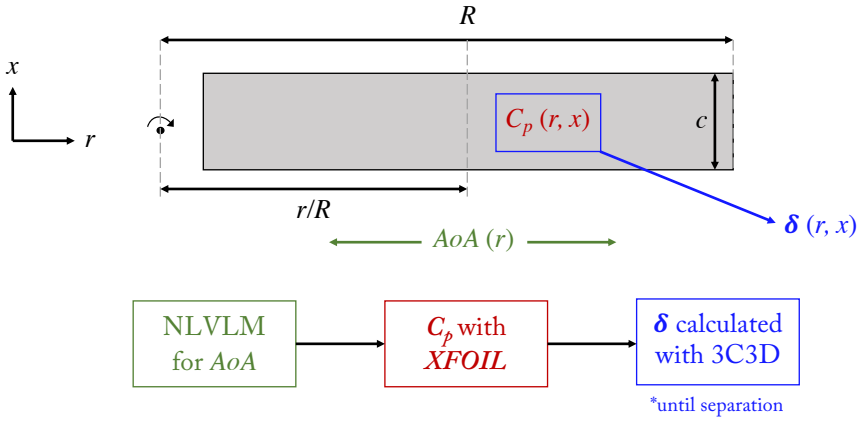

Fig. 3 Schematic of method used to compute local boundary layer thickness

2.2 Roughness Configurations

A frequently used criterion for determining the critical roughness size of three-dimensional roughness was given by Von Doenhoff and Braslow [23]. It is based on a limited body of experimental observations and predicts when a turbulent wedge will form after the roughness element. From Von Doenhoff and Braslow [23] the critical roughness Reynolds number for turbulent wedge formation can be approximated with:

$$Re_{k,crit} \approx 600(d/k)^{2/5} \tag{8}$$

where d denotes the diameter of the roughness element and k, its height. By its nature, such a criterion does not address the shape and distribution of the roughness elements; however, it should suffice for this current work's objectives. In addition to the criteria proposed by Von Doenhoff and Braslow [23], Gregory and Walker [24] conducted experiments using isolated roughness elements at various heights, both smaller and larger than δ. They found that a turbulent wedge would form immediately downstream of the roughness element at $\sqrt{Re_k} \approx 25$. Furthermore, they also studied roughness elements over 2δ and found that the turbulent wedge would increase in spanwise size near the roughness element. Using the data obtained from 3C3D, the range of δ/k along the rotor blade span and the value of $Re_{k,crit}$ for each roughness configuration were calculated (cf. Table 1).

k	$\sqrt{Re_{k,crit}}$	$k/\delta_{3000RPM}$	$k/\delta_{5000RPM}$
52μm	12.92	0.01-0.21	0.11-0.27
78μm	14.02	0.14-0.32	0.17-0.40
140μm	15.75	0.26-0.57	0.31-0.72
220μm	17.25	0.41-0.89	0.48-1.13

Table 1 Summary of roughness configurations tested. Where the range in δ/k corresponds to $r/R = 0.2 - 0.95$. All roughness elements are located at $x/c = 0.1$.

2.3 Freestream turbulence configurations

The freestream turbulence is characterised by its intensity (Tu) and streamwise integral length scale (Λ_u). The integral length scale is the most energetic, corresponding to the average energy-containing eddy's average size. Freestream turbulence was generated using static square grids. Different grid solidities (σ), mesh sizes (M), bar thickness (t), and relative distances between the grid and the leading edge can be used to vary the FST characteristics. In the present work, M was varied to change the levels of turbulence intensity with the value of σ remaining within the range proposed by Kurian and Fransson [25]. All grids were placed at least $15M$ away from the rotor, ensuring the FST is relatively isotropic and homogeneous. The Tu is defined in Eq. 9:

$$Tu = \frac{u_{rms}}{U_0} \tag{9}$$

The Λ_u are calculated by integrating the autocorrelation of their fluctuating velocity signals to the first zero crossing and applying Taylor's hypothesis of frozen turbulence, which converts time scales to spatial scales where $f(\tau)$ is the autocorrelation of the fluctuating velocity signal, and τ is the time delay, *viz*

$$\Lambda_u = U_0 \int_0^\infty f(\tau) d\tau \tag{10}$$

The grid parameters and their corresponding values of Tu and Λ_u are presented in Table 2. The spanwise homogeneity of the turbulence was verified with hotwire measurements; however, for the sake of brevity is not presented here.

Cfg.	$M(mm)$	$t(mm)$	σ	x/M	$Tu(\%)$	$\Lambda_u(mm)$
G1	12	3	38	29	4.91	4.24
G2	23	5	44	15	6.38	8.01

Table 2 Grid and turbulence characteristics at the leading edge of the rotor.

3 Results and Discussion

3.1 Baseline Configuration

The IRT measurements from our previous work for the baseline hover condition at 6500RPM ($Re_{tip} = 144 \times 10^3$) are compared with numerical simulations to gain insight into the flow field and further validate the experimental baseline measurements. Figs. **??** and 4 present a comparison between Shenoy et al. [7] and our results [6]. Shenoy et al. [7] carried out wall-resolved Large Eddy Simulations (LES) of the flow past a NACA0012 rotor at the same c, R, and AoA as in Jaroslawski et al. [6]. The LES results show the formation of an LSB over the suction side over the aerofoil as seen in a slice of the boundary layer flow at $0.8R$ presented in Fig. 4c, corresponding to regions of negative $x-$direction skin friction, $C_{f,x}$. The IRT measurements in Fig. **??**a. show that a separated flow region cools down at a rate much lower than an attached flow [6] corresponding to a region of elevated levels of I_N. The maximum I_N location in a separated flow corresponds to the minimal skin friction value and occurs near the end of the transition process, where further downstream turbulent reattachment could occur. Referring Fig. 4b, the flow topology observed in the experiment has the same characteristics as the LES simulation, consisting of a 3D flow topology and transition front where the latter corresponds to approximately the chordwise location of $\partial I_N/\partial x = 0$ [4, 5, 17, 18]. Near the blade tip, where the local Re is higher, the flow transitions around $x/c = 0.2$ and moves further downstream as r/R decreases (or the local Re). The LES shows that as the outboard region is approached, the LSB has a curved separation line moving closer to the leading edge, resulting in the transition region moving upstream and is due to the variation of the local Reynolds

number and AoA as a function of the radial position. Finally, the LSB is washed out by the tip vortex at the blade tip. The disagreement between the experiment and CFD, notably, the location of $\partial I_N/\partial x = 0$ being further downstream the negative $C_{f,x}$ region is likely due to the rotor rig causing perturbations to the flow, possibly acoustic or mechanical vibrations. These perturbations could excite the boundary layer; a higher initial amplitude would result in a shorter bubble due to the separation position moving downstream and the reattachment position upstream.

A direct comparison between 2D LSBs and the one observed here should be avoided, as a 3D flow is present. However, as found by Toppings and Yaruseyvich [26], LSBs forming over 3D wings have some similarities to 2D bubbles, notably, a roll-up of the separated laminar shear layer into spanwise vortices that subsequently undergo breakdown to turbulence. Moreover, they found that the spanwise flow near the wing tip could increase the initial amplitudes of perturbations in the separated shear layer leading to earlier transition. Additionally, Grande et al. [8] observed through PIV and flow visualisation the formation of an LSB over a MAV propeller in hover and an advancing configuration. A similar 3D transition front was observed, gradually becoming more 2D as the advance ratio (J) increased.

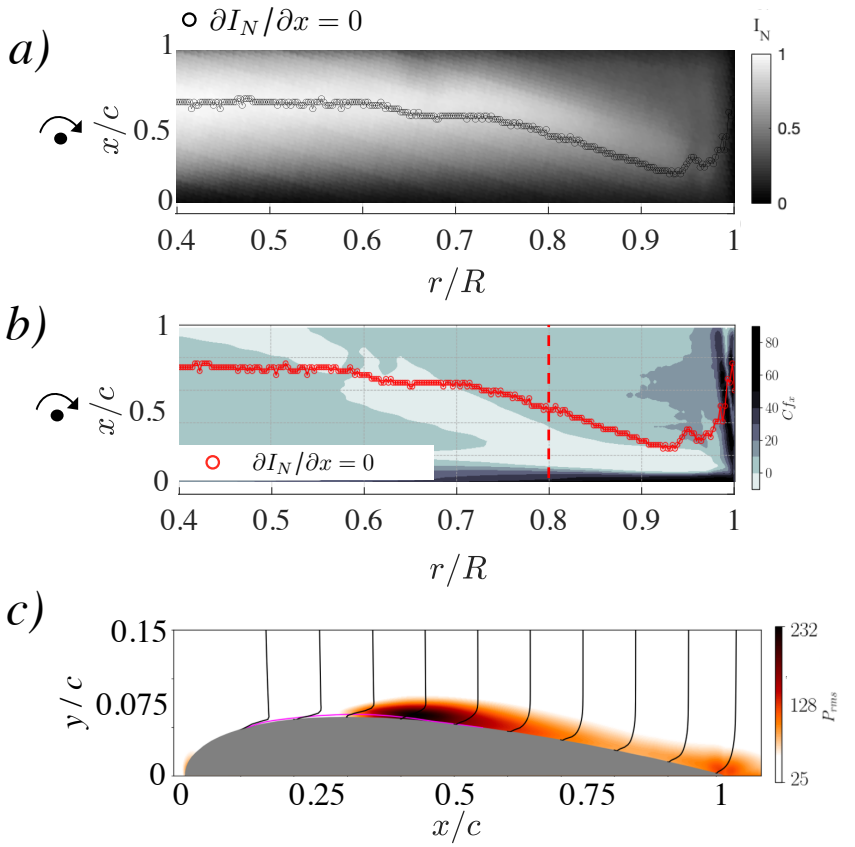

Fig. 4 (a) Normalised IR snapshot from [6] at 6500 RPM (b) The $x-$component skin friction field ($C_{f,x} = \tau_{w,x}/\frac{1}{2}\rho U_{tip}^2$) with the chordwise location of $\partial I_N/\partial x = 0$ as a function of r/R plotted over. (c) Radial slice of the P_{rms} field at $r/R = 0.8$ with the streamwise boundary layer profiles plotted in black and the mean dividing streamline of the laminar separation bubble plotted in magenta.

3.2 Roughness configurations

The coefficients of thrust (C_T) and torque (C_Q), Figure of Merit (FM) and Power loading (PL) are presented in Fig. 5. The magnitudes of the performance metrics are similar in magnitude as for past investigations on micro rotors [27]. Upon further inspection of Fig. 5, it can be observed that the addition of roughness can have a twofold effect on the performance. Roughness elements with smaller heights (52 and 78 μm) show an increase in performance (higher levels of C_T and FM and lower levels of C_Q), whereas those with higher wall-normal distances (140 and 220 μm) deteriorated the performance. Similar behaviour with large roughness elements was observed by Jaroslawski et al. [6], who postulated that extensive roughness elements could cause increased

levels of excrescence drag. The performance increase results from laminar separation suppression due to the roughness elements promoting earlier transition. Reducing the size of an LSB or the separation zone has resulted in less profile drag and performance gains, as numerical studies by Jung and Baeder [10] and Argus et al. [11] have shown.

The IR snapshots of the flow topology over the rotor for each roughness configuration, along with the radial evolution of the roughness Reynolds number (Re_k) at $x/c = 0.1$ are presented in Fig. 6. The IR snapshots show the formation of wakes behind the roughness elements and, at a critical value of Re_k, break down into turbulent wedges, which merge into a transition front. Referring to Fig. 6, the Von Doenhoff and Braslow [23] criterion (cf. $Re_{k,crit}$ in Table. 1) can indicate when roughness elements cause the flow to transition. For example, at $Re_{tip} = 66 \times 10^3$ $(3000\ RPM)$ Re_k does not reach a critical value for roughness heights of 52 and 78μm resulting in no clear wedge formation behind the roughness elements (cf. Fig. 6a). However, increasing Re_{tip} to 110×10^3 $(5000\ RPM)$ increases the Re_k to a critical value for the 78μm configuration, resulting in wedge formation at approximately the critical value of 14.02, based on the correlation proposed by Von Doenhoff and Braslow [23]. The validity of this criterion over a boundary layer flow developing over a low Reynolds number rotor was first demonstrated by Jaroslawski et al. [6], and here we extend the findings and show that this criterion is also valid for various roughness heights. Additionally, the performance increase is only present when $Re_k < Re_{k,crit}$, suggesting $Re_{k,crit}$ could be used as a threshold for overtripping in terms of performance.

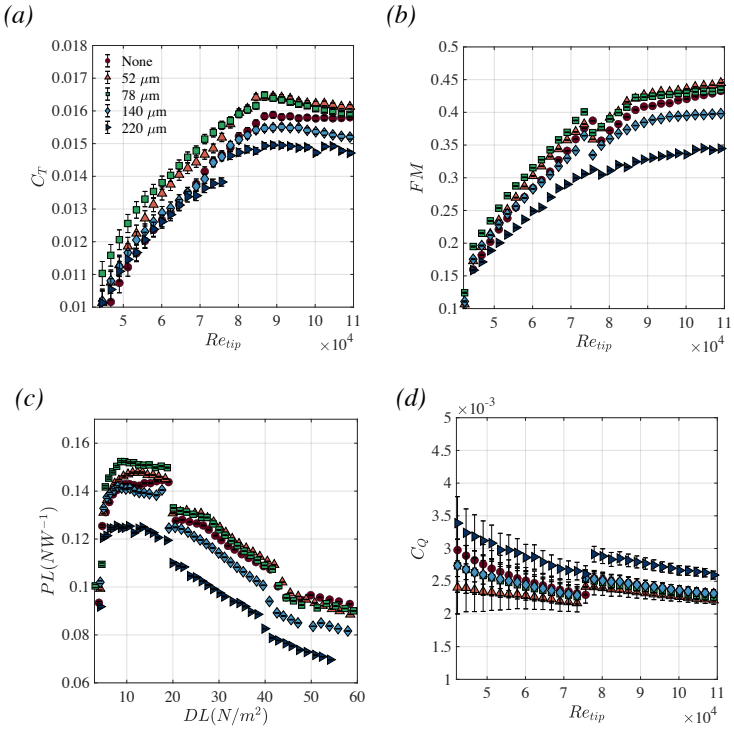

Fig. 5 (a) The coefficient of thrust (C_T), (b) Figure of Merit (FM), (c) Power Loading (PL) and (d) the coefficient of torque (C_Q) for the rotor in the hover configuration for different heights of 3D roughness elements. Rotation speeds: 2000–5000 RPM

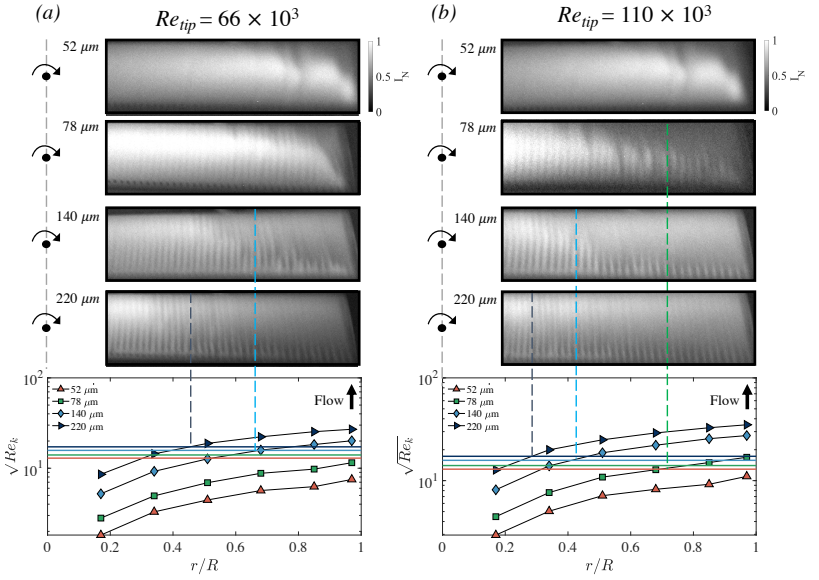

Fig. 6 IR snapshots of roughness configurations at (a) $Re_{tip} = 66 \times 10^3$ (3000 RPM) and (b) $Re_{tip} = 110 \times 10^3$ (5000 RPM). Local Re_k is compared to $Re_{k,crit}$, with coloured lines corresponding to the radial position where $Re_{k,crit}$ occurs.

3.3 Freestream turbulence configurations

Besides operating in a different flight configuration, the significant difference between this experiment and one in the previous section is that the introduction of roughness leads to a non-negligible excrescence drag if the critical height had not been chosen carefully, as in the case of the roughness protruding the outside the boundary layer. On the other hand, freestream turbulence can perturb the boundary layer without adding additional excrescence drag, as with roughness.

The characterisation of the freestream turbulence is presented in Fig 7, where the streamwise evolution of the Tu (cf. Fig. 7a) shows the conventional exponential decay being present before the leading edge of the rotor. Additionally, the integral length scales also increased in size further away from the grid (not presented here). The Power Spectral Density (PSD) in Fig .7b, of the streamwise fluctuating velocity, exhibits a broader inertial sub-range for the configuration with a higher level of Tu, which is coherent with the values of Λ_u. Referring to Fig. 7c, the mean streamwise freestream velocity upstream of the rotor showed negligible variation in the spanwise direction. Referring to Fig. 7d, the drag force on the rig with the static rotor is effectively the same for the freestream velocity used for the experiments (U_o= 3.5 m/s) for an upstream flow with and without grid-generated FST. Therefore, freestream turbulence is insignificant to the drag of the static setup and hence will not introduce any bias into force measurements. However, at higher speeds, the presence of

freestream turbulence does increase the drag on the static rig, suggesting the application of corrections at higher inflow velocities.

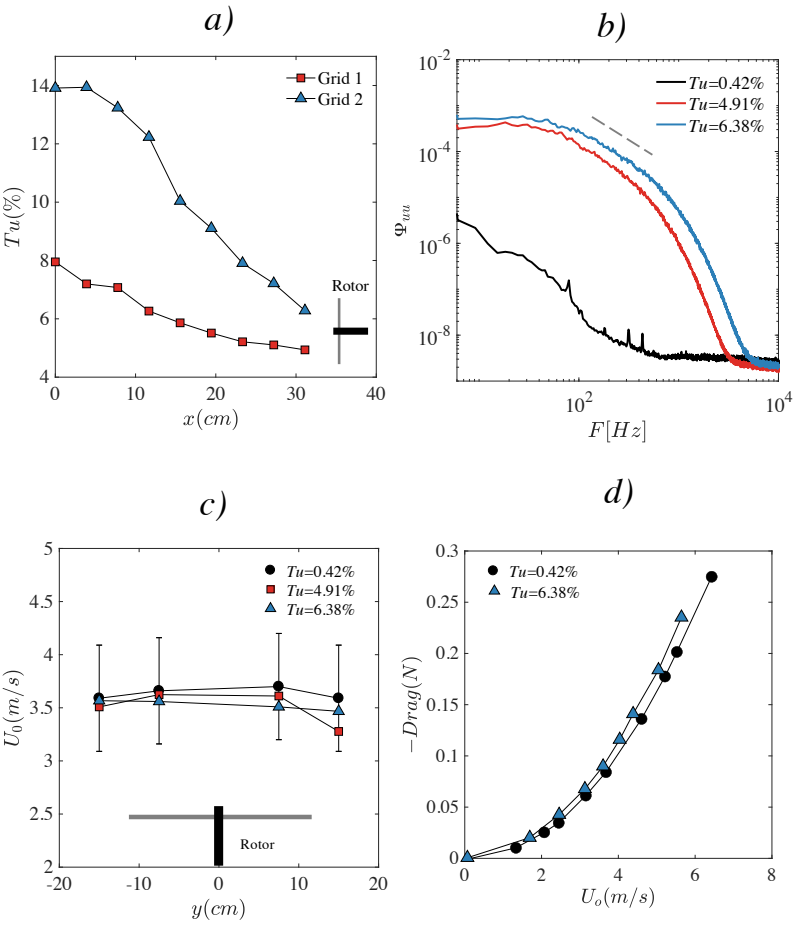

Fig. 7 a) Freestream turbulence. b) PSD ($m^s/s^2/Hz$) for all flow configurations at the rotor. c) Mean flow homogeneity for each flow configuration. d) Effect of freestream turbulence on the static rig.

Referring to the coefficients of thrust (C_T) and torque (C_Q) and efficiency (η) in Fig. 8, the values are of similar magnitude as in recent studies on low Reynolds number propellers [28], in general, increasing the level of freestream turbulence improves the performance. At lower RPM, the effects of FST on the C_T are less pronounced, whereas, at $Re_{tip} = 60 - 80 \times 10^3$ ($0.35 < J < 0.3$), there is a slight decrease in the evolution of C_T with no effects of FST. This behaviour could be due to the local angle of incidence not being positive along the entire span of the rotor in this range of Re_{tip}. Referring to Fig. 9 at low values of J, there is a large portion of the blade with a negative

angle of attack, which explains the low-performance values. The decrease in performance when $0.3 > J > 0.35$ could be caused by a larger separation region due to the relatively low effective angles of attack and low local Reynolds numbers near the blade's root. However, this hypothesis cannot be confirmed based on the current measurements. Once $Re_{tip} > 80 \times 10^3$ ($J < 0.3$), the angle of attack is positive along the large potions of the rotor's span, and the effects of FST become more pronounced. Moreover, it is important to note that, since more thrust is produced, the induced power and torque increase. If this is not accounted for, the measured torque value will contain the induced torque due to higher thrust. Therefore, the induced torque ($Q_{in} = (U_o + v_i) \times T$ where v_i is the induced velocity and is obtained from Froude's theory: $v_i = \sqrt{T/2\pi R^2}$) is subtracted from the measured torque and should give a more accurate measure of profile drag on the rotor. The decrease of C_Q with an increase of RPM is due to the blade's section angle of attack reducing below the stall angle; hence the torque decreases due to less drag. As expected, the propulsive efficiency exhibits an opposite trend: whilst the torque decreases, the propulsive efficiency increases.

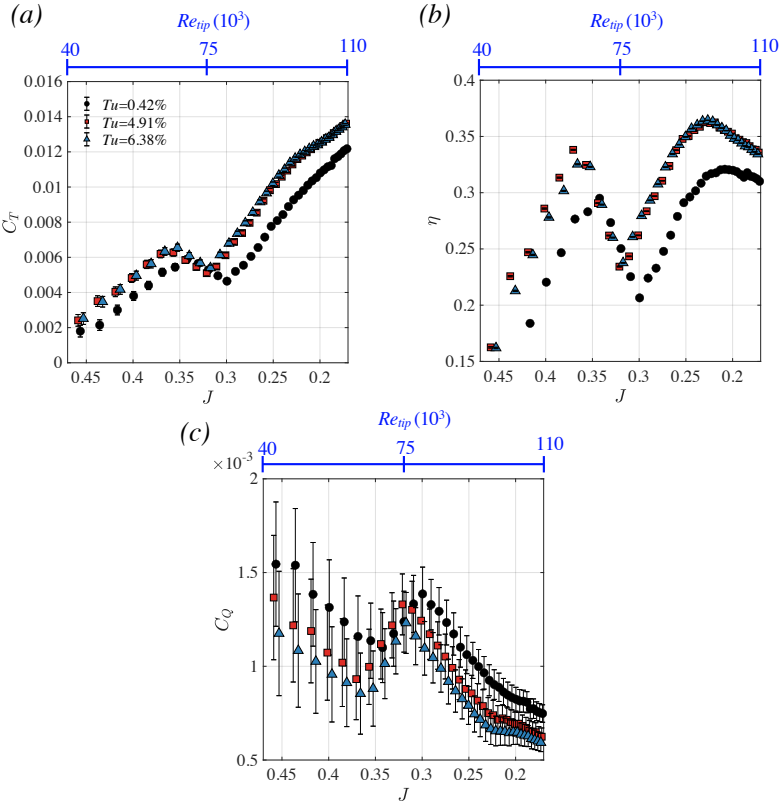

Fig. 8 (a) The coefficient of thrust (C_T), (b) efficiency (η) and (c) the coefficient of torque (C_Q) for the rotor in the climbing configuration for a fixed $U_o = 3.5$ m/s varying the rotation speeds from 2000−5000 RPM for the three upstream flow configurations.

The mechanism behind the performance increase cannot be fully explained based on the current measurements. However, based on the low range of Reynolds numbers and previous investigations [9, 11] boundary layer separation suppression is the possible cause in the current configuration, leading to a hypothesis that the FST is interacting with the boundary layer developing over the rotor. The increased perturbation in the boundary layer would accelerate the transition to turbulence, which would, in turn, delay or suppress flow separation. The suppression of separation increases thrust levels resulting in lower levels of drag in the thrust component, which is also observed with the lower levels of torque with increasing Tu.

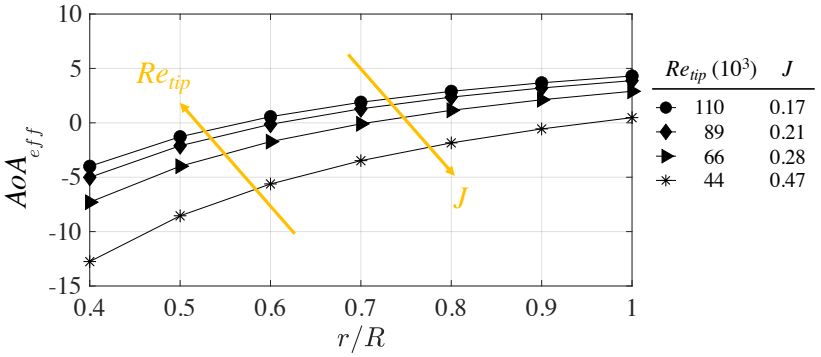

Fig. 9 Effective angle of attack (AoA_{eff}) as a function of radial position (r/R) calculated from momentum theory.

IRT measurements are conducted for the natural flow case ($Tu = 0.42\%$) and the highest turbulence case ($Tu = 6.38\%$) are presented in Fig. 10 for $Re_{tip} = 89 \times 10^3$ (4000 RPM) at $U_o = 3.5\ m/s$. The flow topology is different from the configuration in hover as the addition of freestream flow reduces the local AoA, hence modifying the boundary layer development. The lower AoA would delay any boundary layer separation, which in turn would cause boundary layer transition to occur later. In other words, as U_o increases (effectively increasing the advance parameter, J), the velocity at the suction side decreases, and the stagnation point moves toward the leading edge, corresponding to a reduction in AoA. Therefore, the boundary layer flow over the rotor is significantly different than a hover configuration for the same RPM but still highly susceptible to separation. For instance, Grande et al. [8] found that the streamwise and spanwise length of the LSB increased with the advance parameter where at $J = 0.6$, separation without reattachment was observed. This observation is likely due to the local angle of attack decreasing with J, reducing the extent of the streamwise adverse pressure gradient, causing separation to occur later, and resulting in no reattachment.

Referring to Fig. 10c, the maximum value of I_N is shifted upstream when the freestream turbulence increases, corresponding to an earlier transition front. These results show that the freestream turbulence interacts with the boundary layer, suggesting that the changes in C_T and η could be related to boundary layer transition. When subjected to sufficiently high levels of FST ($Tu > 1\%$), the transition mechanisms in attached boundary layer flow [29], and LSBs [3, 30] contain the presence of non-modal instabilities manifesting themselves as streaks. IRT measurements of streaks at subsonic flows are not a trivial task. The temperature difference between the low and high momentum regions in the streaks is expected to be an order of magnitude lower than that of the temperature gradient between a laminar and turbulent flow, which already approaches the temperature NETD of the IR camera (for example, at Mach = 0.1 and $300K$, the temperature difference between laminar and turbulent is around $30-40\ mK$).

Therefore, the possible mechanism of a performance increase could be suppression/modification of the separated flow region, which could increase performance. It is essential to specify that these are standalone measurements and any direct comparisons between the results for measurements of the rotor in hover are thus not appropriate. Finally, the particularity of this boundary layer forcing method is that it is only limited to when the rotor operates in advancing or climbing configurations, as FST is not achievable without an incoming velocity.

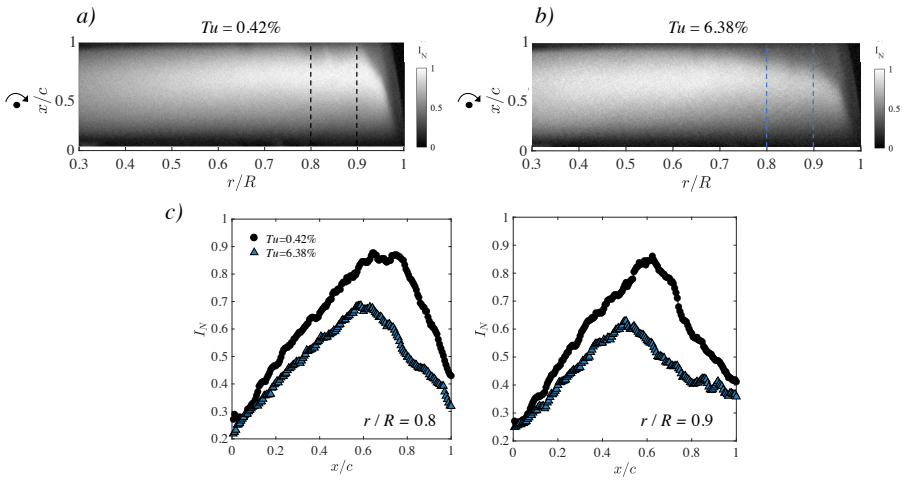

Fig. 10 IRT snapshots of the suction side of one of the rotors aerofoils for a) no additional FST and b) $Tu = 6.38\%$. c) Chordwise evolution of I_N at $r/R = 0.8$ and 0.9, for both configurations. $Re_{tip} = 89 \times 10^3$ (4000 RPM) for both cases.

4 Conclusion

Phase-locked Infrared thermography, force, and torque measurements on a rotor operating at low Reynolds numbers ($10^3 - 10^5$) were conducted. Two separate experiments studying the effects of forcing the boundary layer with roughness or freestream turbulence revealed that:

1. In a hover configuration, 3D roughness placed at $x/c = 0.10c$ can have a twofold effect on the performance, with the value of Re_k being a critical parameter. The low order boundary layer calculation proved to be useful as it helped in defining the roughness height and the limit where it became supercritical. A series of roughness heights ranging from subcritical to critical were tested to check if the criterion proposed by Von Doenhoff and Braslow [23] can be extended to a 3D flow over a rotor. Configurations with values of $Re_k < Re_{k,crit}$ were found to increase performance, suggesting that when $Re_k \approx Re_{k,crit}$ the excrescence drag caused by the roughness can be detrimental. Hence, this semi-empirical criterion can still be used as

an indicator for transition into fully developed wedges behind 3D roughness and can be a good starting point for the design of passive flow control devices for low Reynolds number rotors. The mechanisms of a performance increase could be due to delay/suppression of boundary layer separation as suggested by [10, 11].

2. In an advancing configuration, freestream turbulence can increase the performance (C_T, η and C_Q) of a rotor operating at low Reynolds numbers ($40000 < Re < 110000$). Notably, the performance gain was 8% in terms of C_T and 6% in terms of η at $J = 0.22$ or $Re_{tip} \approx 93 \times 10^3$. The possible mechanisms behind the performance increase could be a delay/suppression of boundary layer separation via freestream turbulence exiting the boundary layer, resulting in lower levels of C_Q due to less profile drag from separation reduction/suppression. This is supported by IRT measurements which show that the addition of FST advances the transition front and decreases the magnitude of I_N. Due to the insufficient temperature resolution of the camera, more details on the flow topology, such as streaks, could not be measured. However, it can be concluded that the freestream turbulence interacts with the boundary layer.

The present results demonstrate that exciting the boundary developing layer over the suction side of a NACA0012 rotor operating at low Reynolds numbers can increase the performance by forcing transition with FST or 3D roughness elements. In particular, the FST is efficient in boundary layer forcing as the boundary layer is perturbed without adding excrescence drag as roughness elements, where an incorrectly designed element can decrease the performance. However, the current results also suggest that designing an optimal roughness trip can increase performance. Even if this study was conducted for a non-optimised rotor, recent developments in the literature show the presence of flow separation and LSBs on more realistic micro drone rotors and propellers. Therefore the current results are encouraging, as here we demonstrate that controlling boundary layer transition can provide performance gains, paving the way for future parametric studies and design optimisation.

5 Declarations

5.1 Ethical Approval

N/A

5.2 Competing interests

The authors have no conflicts of interest to declare that are relevant to the content of this article.

5.3 Authors' contributions

All authors contributed to the publication of this manuscript.

5.4 Funding

Funding supported by an ONERA internal project and ISAE-SUPAERO.

5.5 Availability of data and materials

Data can be made available upon reasonable request.

References

[1] Gaster, M.: The structure and behaviour of laminar separation bubbles. Tech. Rep. Aeronautical Research Council Reports and Memoranda 3595 (1967)

[2] Marxen, O., Henningson, D.S.: The effect of small-amplitude convective disturbances on the size and bursting of a laminar separation bubble. Journal of Fluid Mechanics **671**, 1–33 (2011)

[3] Hosseinverdi, S., Fasel, H.: Numerical investigation of laminar–turbulent transition in laminar separation bubbles: the effect of free-stream turbulence. Journal of Fluid Mechanics **858**, 714–759 (2019)

[4] Thiessen, R., Schülein, E.: Infrared thermography and dit of quadcopter rotor blades using laser heating. In: Multidisciplinary Digital Publishing Institute Proceedings, vol. 27, p. 31 (2019)

[5] Lang, W., Gardner, A., Mariappan, S., Klein, C., Raffel, M.: Boundary-layer transition on a rotor blade measured by temperature-sensitive paint, thermal imaging and image derotation. Experiments in Fluids **56**(6), 118 (2015)

[6] Jaroslawski, T., Forte, M., Moschetta, J.-M., Delattre, G., Gowree, E.R.: Characterisation of boundary layer transition over a low Reynolds number rotor. Experimental Thermal and Fluid Science **130**, 110485 (2022)

[7] Vittal Shenoy, D., Gojon, R., Jardin, T., Jacob, M.C.: Aeroacoustic study of low Reynolds/low Mach number rotor using les. In: Aero 2022 56th 3AF International Conference on Applied Aerodynamics, Toulouse, France, pp. 44–2022 (2022)

[8] Grande, E., Romani, G., Ragni, D., Avallone, F., Casalino, D.: Aeroacoustic investigation of a propeller operating at low reynolds numbers. AIAA Journal **60**(2), 860–871 (2022)

[9] Singh, R.K., Ahmed, M.R.: Blade design and performance testing of a small wind turbine rotor for low wind speed applications. Renewable Energy **50**, 812–819 (2013)

[10] Jung, Y.S., Baeder, J.: Simulations for effect of surface roughness on wind turbine aerodynamic performance. In: Journal of Physics: Conference Series, vol. 1452, p. 012055 (2020). IOP Publishing

[11] Argus, F.J., Ament, G.A., Koning, W.J.: The influence of laminar-turbulent transition on rotor performance at low Reynolds numbers. VFS Technical Meeting on Aeromechanics for Advanced Vertical Flight,San Jose, CA, January 21– 23 (2020)

[12] Koning, W.J., Romander, E.A., Johnson, W. Annual American Helicopter Society International Forum and Technology Display, Phoenix, Arizona, May 14-17 (2018)

[13] Bruun, H.H.: Hot-wire anemometry: principles and signal analysis. IOP Publishing (1996)

[14] Desert, T., Moschetta, J., Bezard, H.: Aerodynamic design of a martian micro air vehicle. In: Proceedings of the 7th European Conference for Aeronautics and Aerospace Sciences (2017)

[15] Schäfer, P., Severin, J., Herwig, H.: The effect of heat transfer on the stability of laminar boundary layers. International journal of heat and mass transfer **38**(10), 1855–1863 (1995)

[16] Raffel, M., Merz, C.B.: Differential infrared thermography for unsteady boundary-layer transition measurements. AIAA journal **52**(9), 2090–2093 (2014)

[17] Miozzi, M., Capone, A., Costantini, M., Fratto, L., Klein, C., Di Felice, F.: Skin friction and coherent structures within a laminar separation bubble. Experiments in Fluids **60**(1), 13 (2019)

[18] Wynnychuk, D.W., Yarusevych, S.: Characterization of laminar separation bubbles using infrared thermography. AIAA Journal **58**(7), 2831–2843 (2020)

[19] Drela, M.: XFOIL: An analysis and design system for low Reynolds number airfoils, 1–12 (1989)

[20] Jo, Y., Jardin, T., Gojon, R., Jacob, M.C., Moschetta, J.-M.: Prediction of noise from low Reynolds number rotors with different number of blades using a non-linear vortex lattice method. In: 25th AIAA/CEAS Aeroacoustics Conference, p. 2615 (2019)

[21] Houdeville, R.: Three-dimensional boundary layer calculation by a characteristic method. In: Fifth Symposium on Numerical and Physical Aspects of Aerodynamic Flows, Long Beach, January 1992 (1992)

[22] Perraud, J., Vermeersch, O., Houdeville, R.: Descriptif et mode d'emploi du code 3c3d. ONERA, RT **1**, 18325 (2011)

[23] Von Doenhoff, A.E., Braslow, A.L.: The effect of distributed surface roughness on laminar flow, 657–681 (1961)

[24] Gregory, N., Walker, W.: The Effect on Transition of Isolated Surface Excrescences in the Boundary Layer. HM Stationery Office, ??? (1956)

[25] Kurian, T., Fransson, J.H.: Grid-generated turbulence revisited. Fluid dynamics research **41**(2), 021403 (2009)

[26] Toppings, C.E., Yarusevych, S.: Structure and dynamics of a laminar separation bubble near a wing root: towards reconstructing the complete lsb topology on a finite wing. Journal of Fluid Mechanics **944** (2022)

[27] Bohorquez, F.: Rotor hover performance and system design of an efficient coaxial rotary wing micro air vehicle (2007)

[28] Veismann, M., Yos, D., Gharib, M.: Parametric study of small-scale rotors in axial descent. Physics of Fluids **34**(3), 035124 (2022)

[29] Fransson, J.H., Shahinfar, S.: On the effect of free-stream turbulence on boundary-layer transition. Journal of Fluid Mechanics **899** (2020)

[30] Jaroslawski, T.M., Forte, M., Vermeersch, O., Gowree, E.R., Moschetta, J.-M.: On the multi-modal growth of disturbances in a laminar separation bubble subjected to freestream turbulence. To appear in: 12th International Symposium on Turbulence and Shear Flow Phenomena. Osaka, Japan, July 19–22 (2022)